Dynamic analysis of coupled wind-train-bridge system considering tower shielding and triangular wind barriers

Nan Zhang[*1,2], Guanghui Ge[1a], He Xia[1b] and Xiaozhen Li[3c]

[1]School of Civil Engineering, Beijing Jiaotong University, Beijing 100044, China
[2]Beijing Key Laboratory of Structure Wind Engineering and Urban Wind Environment, Beijing 100044, China
[3]School of Civil Engineering, Southwest Jiaotong University, Chengdu 610031, China

Abstract.   A method for analyzing the coupled wind-vehicle-bridge system is proposed that also considers the shielding effect of the bridge tower with triangular wind barriers. The static wind load and the buffeting wind load for both the bridge and the vehicle are included. The shielding effects of the bridge tower and the triangular wind barriers are incorporated by taking the surface integral of the wind load. The inter-history iteration is adopted to solve the vehicle-bridge dynamic equations with time-varying external loads. The results show that after installing the triangular wind barriers in the area of the bridge tower, the bridge response and the vehicle safety factors change slightly. The peak value of the train car body acceleration is significantly reduced when the wind barrier size is increased.

Keywords: suspension bridge; vehicle-bridge interaction; wind load; wind barrier

1. Introduction

In recent years, more suspension bridges are constructed for railways, especially in high-speed railways, as shown in Table 1. The suspension bridges fulfill the requirement of span length, which exceeds all other types of bridges, while the vertical and lateral stiffness of this type of bridge is quite low, so the wind loads plays an important role for the dynamic behavior of both the bridge and the passing trains.

There has been significant research on the vehicle-bridge coupled system considering the wind loads. In addition to the traditional modeling method of the vehicle-bridge system, the wind speed fields for both the bridge and the vehicle were simulated with the wind effects expressed by time-varying forces and moments. The wind load on the bridge subsystem can be separated into a static wind load, a buffeting wind load, and a self-excited wind load. Lin and Yang (1983) simulated the load history of the wind field as a function in time domain and then calculated the bridge dynamic performance with a time history integral. Many researchers adopted a similar

---

method to study the vibrations of a bridge. Xu and Zhu (2005) established a nonlinear finite element model (FEM) for the Tsing Ma Suspension Bridge and compared the computed acceleration responses of the bridge deck and cable in crosswinds with experimental data. Chen (2011) proposed a framework for dynamic stress analysis of long suspension bridges under wind, railway, and highway loadings, and compared predicted stresses with measured data. Kim (2014) developed a computational fluid dynamics (CFD) program with fluid-structure interaction (FSI) to perform a buffet analysis of a 3D cable-stayed bridge, including the calculation of the dynamic responses and detailed wind flows. Zhang (2011) presented an approach of full-mode aerodynamic flutter analysis for long-span suspension bridges, which considered the nonlinearities of structural, aerostatic, and aerodynamic forces. It used FEM to compute the deformation under the static wind loading and flutter loads in both the time domain and frequency domain. Domaneschi (2014) proposed an updated numerical model of a suspension bridge in a commercial finite element work frame and adopted a more refined version of the wind-structure interaction forces. Han (2012) established an experimental setup to measure the aerodynamic characteristics of vehicles and the bridge considering the wind turbulence, wind speed, vehicle interference, and vehicle position. Results were validated by comparing surface pressure measurements on the vehicle and the bridge with fundamental derivations. Cai (2013) proposed a three-dimensional finite element analysis framework to solve the wind-vehicle-bridge interaction that includes moving vehicles. Cao *et al.* (2000) simulated the time-space domain wind velocity field for long span bridges, where the wind load on the vehicle subsystem consisted of the steady and unsteady wind loads.

Ge (2014) studied the wind field parameters and the aerodynamic response characteristics of long-span bridges during a typhoon landfall. Baker (1991a, b, c) summarized prior research and proposed a systematic method to generate the force and moment histories for moving trains. Building on Baker's method, Xu *et al.* (2004) presented a proposed framework and the computer program to predict the dynamic response of coupled train and cable-stayed bridge systems subjected to cross winds.

Table 1 Suspension bridges with railways

Bridge	Span /m	Railway/ Highway	Open Year
Washington Bridge, USA	1067	4/8	1931
San Francisco Bay Bridge, USA	705	2/6	1936
Naruto Bridge, Japan	876	2/6	1985
Shimotsui-Seto Bridge, Japan	940	4/4	1987
Minami Bisan-Seto Bridge, Japan	1100	4/4	1988
Kita Bisan-Seto Bridge, Japan	990	4/4	1988
Tsing Ma Bridge, China	1377	2/6	1997
April 25th Bridge, Portugal	1013	2/6	1999
Bosporus 3rd Bridge, Turkey	1408	2/6	Under construction
Messina Strait Bridge, Italy	3300	2/8	Under construction
Jinsha River Bridge, China	660	2/0	Under construction
Wufengshan Bridge, China	1036	2/8	Under construction

Guo *et al.* (2010) analyzed the dynamic responses of the Tsing Ma suspension bridge with trains running on the bridge under turbulent wind conditions to propose a threshold curve of safe wind velocity for trains on the bridge. In order to simulate the motion of road vehicles, Wang (2014a) calculated aerodynamic parameters from CFD under the special condition of vehicles passing by an obstacle (2014b). Li (2014) measured aerodynamic forces and moments on a vehicle and bridge deck when the vehicle model moved on the bridge deck under crosswinds in a large wind tunnel. The test considered different vehicle speeds, wind yaw angles, rail track positions, and vehicle types.

Li *et al.* (2005) described the shielding effect for obstacles of bridge members, which may cause sudden loads and an increased possibility of train derailment and overturning. It was found that derailment and offload factors of the train increase greatly when the train passes by the bridge tower of a cable-stayed bridge. In order to mitigate the shielding effect, one solution is to install the wind barriers on the bridge to block the train from direct wind load (Gao 2014). However, the wind barriers increase the designing wind load of the bridge, thus requiring larger member sections. This leads to larger amounts of construction material. As an alternative solution, this paper proposes a wind barrier of triangular shape. A barrier of this type has been developed by analyzing the dynamic responses and the running safety indexes of a train on the bridge.

2. Aerodynamic loads with wind barriers

The vehicle-bridge coupled system consists of a vehicle subsystem and a bridge subsystem. Both subsystems are excited by the wind loads, track irregularities, and the dynamic loads from the moving vehicles.

The wind loads on the bridge subsystem and the vehicle subsystem are calculated based on aerodynamic parameters, which are obtained from wind tunnel experiments or CFD calculations. Using the method proposed by Li *et al.* (2013), the parameters of the bridge and the vehicle can be measured separately. Thus, the wind loads on both bridge and vehicle are derived independently as follows.

The static wind force induces a long wavelength deformation of the bridge deck. For a long span bridge, the curvature caused by the static wind load is small and can be neglected. However, the span-to-span angle at the bridge ends affects the local irregularity of the track, which may increase the probability of derailment and overturning of the vehicle. Therefore, the static wind load must be considered in the coupled wind-vehicle-bridge system. For each bridge node, the static wind load is

$$\begin{Bmatrix} F_{y0} \\ F_{z0} \\ M_{x0} \end{Bmatrix} = \frac{1}{2}\rho U^2 L \begin{Bmatrix} C_D D \\ C_L B \\ C_M B^2 \end{Bmatrix} \tag{1}$$

where F_{y0}, F_{z0}, and M_{x0} are the lateral, vertical, and torsional components of the static wind loads, respectively. The air density is ρ and the wind velocity is U at the bridge deck. C_D, C_L, and C_M are the aerodynamic parameters of bridge deck beam, where D, B, and L are the height (along the vertical direction), width (along the lateral direction of the bridge) and nodes distance (along the longitudinal direction) of the bridge deck, respectively.

The static wind force causes a constant trend of offload and overturning to the train vehicle. This force can also be calculated with Eq. (1), but the dimensions of *D*, *B,* and *L* are taken as the height, width, and length of a train vehicle, respectively.

The buffeting wind force induces vibration of the bridge and train vehicle. It acts on the bridge nodes and the center of gravity (CG) of the vehicle car body. The buffeting wind force can be expressed as

$$
\begin{Bmatrix} F_{y1} \\ F_{z1} \\ M_{x1} \end{Bmatrix} = \frac{1}{2}\rho U^2 BL \begin{Bmatrix} 2C_D\dfrac{u(t)}{U}+C_D^{'}\dfrac{w(t)}{U} \\ 2C_L\dfrac{u(t)}{U}+\left(C_L^{'}+C_D\right)\dfrac{w(t)}{U} \\ 2C_M B\dfrac{u(t)}{U}+C_M^{'}B\dfrac{w(t)}{U} \end{Bmatrix} \tag{2}
$$

where F_{y1}, F_{z1}, and M_{x1} are the lateral, vertical, and torsional components of the buffeting wind loads, respectively. C'_D, C'_L, and C'_M are the derivatives of aerodynamic parameters with respect to the wind attack angle α at $a=0$; and $u(t)$ and $w(t)$ are the buffeting components of wind velocities in lateral and vertical directions, respectively. The dimensions D, B, and L for bridge and vehicle are the same as in Eq. (1).

To analyze the shielding effect of triangular wind barriers on a bridge tower, the wind load on the car-body is shown in Fig. 1. X is the position of the vehicle; S_c and H_c are the length and height of the car-body, respectively. S_t is the width of bridge tower. S_b and H_b are the width and height of the wind barrier, respectively. The area subjected to wind load is modeled as a pentagon whose vertical sides are a and c, with lateral sides b and d.
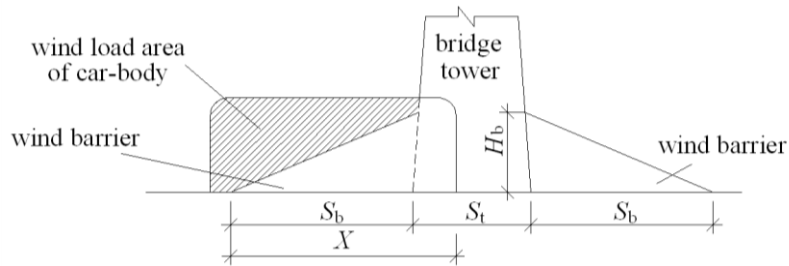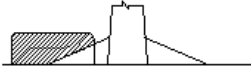

(a) Shielding effect of the bridge tower and wind barrier
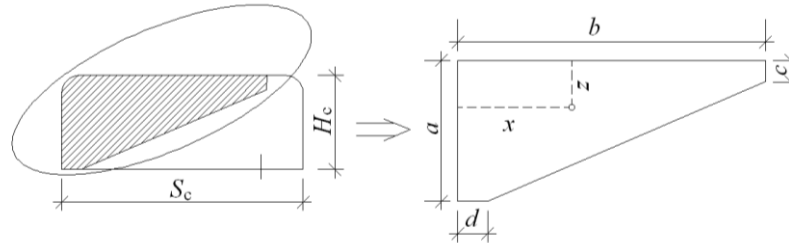
(b) Wind load area of car-body

Fig. 1 Shielding effect and wind load area of car-body

Table 2 Stages of a train running through the shielded area

Stages	X	SB: $S_c-S_t\leq S_b\leq S_c$	LB: $S_b\geq S_c$
Stage 1	SB: $0\leq X<S_b$ LB: $0\leq X<S_c$		
Stage 2	SB: $S_b\leq X<S_c$ LB: $S_c\leq X<S_b$		
Stage 3	SB: $S_c\leq X<S_b+S_t$ LB: $S_b\leq X<S_b+S_t$		
Stage 4	SB & LB: $S_b+S_t\leq X<S_b+S_c$		
Stage 5	SB: $S_b+S_c\leq X<2S_b+S_t$ LB: $S_b+S_c\leq X<S_b+S_t+S_c$		
Stage 6	SB: $2S_b+S_t\leq X<S_b+S_t+S_c$ LB: $S_b+S_t+S_c\leq X<2S_b+S_t$		
Stage 7	SB: $S_b+S_t+S_c\leq X\leq 2S_b+S_t+S_c$ LB: $2S_b+S_t\leq X\leq 2S_b+S_t+S_c$		

The process of a train vehicle passing through the shielded area is divided into seven stages, as described in Table 2. It is distinguished by cases with a short barrier ($S_c-S_t\leq S_b\leq S_c$, expressed as SB) and a long barrier ($S_b\geq S_c$, expressed as LB). A wind barrier with very short length is seldom used in bridge engineering, so the case of $S_b<S_c-S_t$ is not addressed in this paper.

To calculate the wind loads on the car-body, the following approach was used. In the bridge designing codes *Fundamental Code for Design on Railway Bridge and Culvert* (Chinese code TB10002.1-2005); *Steel, concrete and composite bridges - Part 2: Specification for loads* (British code BS5400-2: 2006); and *Actions on structures, Part 1-4: General actions, Wind actions* (European code EN 1991-1-4: 2005); the vehicle wind load is taken into consideration and defined in proportion to the car-body side area. This implies that the wind load on car-body uniform distribution on the body. Thus, the wind loads acting on the vehicle can be expressed by the surface integral

$$\begin{Bmatrix} F_y \\ F_z \\ M_x \\ M_y \\ M_z \end{Bmatrix} = \frac{1}{S_c H_c} \begin{Bmatrix} \int_A \left(F_{y0}+F_{y1}\right)dA \\ \int_A \left(F_{z0}+F_{z1}\right)dA \\ \int_A \left(M_{x0}+M_{x1}+F_{y0}z_A+F_{y1}z_A\right)dA \\ \left(F_{z0}+F_{z1}\right)x_A dA \\ \left(F_{y0}+F_{y1}\right)x_A dA \end{Bmatrix} \tag{3}$$
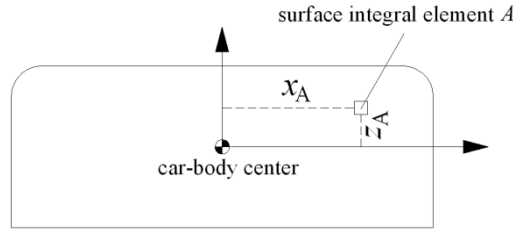
Fig. 2 Surface integral of wind load

where F_y and F_z are the lateral and vertical forces, respectively, acting on the car-body CG. M_x, M_y, and M_z are the moments about x (the train running direction), y (lateral direction), and z (vertical direction) axes, respectively, acting on the car-body CG. Finally, x_A and z_A are the coordinates of surface element A relative to the car-body CG, as shown in Fig. 2.

As shown in Fig. 1(b), the wind load area of the car-body can be calculated with the coordinates x and z relative to the area CG

$$\begin{cases} x = \dfrac{3cb^2 + 3d^2(a-c) + (a-c)(b-d)(b+2d)}{3(ab+ad+bc-cd)} \\ z = \dfrac{3bc^2 + 3(a^2-c^2)d + (a-c)(b-d)(a+2c)}{3(ab+ad+bc-cd)} \end{cases} \tag{4}$$

To express the size of the wind load area, a parameter is introduced. This is the ratio of wind load area to the side surface of car-body

$$\beta = \frac{ab+ad+bc-cd}{2H_c S_c} \tag{5}$$

In Stages 1 to 3, only one area in the rear part of the car-body is subjected to the wind load. In Stage 4, two areas in both the rear and the front parts of the car-body are subjected to the wind load. Since the structures of wind barriers and bridge tower are symmetric, the wind loads are repeated in a reverse order as the vehicle passes through Stages 5 to 7. The side lengths a, b, c, and d are listed in Table 3. The values for SB and LB in Stage 2 are different and are, therefore, listed separately.

Table 3 Side lengths for Stages 1 to 4

Stage / Part	a	B	c	d
1	H_c	S_c	$H_c - X H_b / S_b$	$S_c - X$
2, SB	H_c	$S_b - X + S_c$	$H_c - H_b$	$S_c - X$
2, LB	$H_c - (X - S_c) H_b / S_b$	S_c	$H_c - X H_b / S_b$	0
3	$H_c - (X - S_c) H_b / S_b$	$S_b - X + S_c$	$H_c - H_b$	0
4, rear part	$H_c - (X - S_c) H_b / S_b$	$S_b - X + S_c$	$H_c - H_b$	0
4, front part	$H_c - (2S_b + S_t - X) H_b / S_b$	$X - S_b - S_t$	$H_c - H_b$	0

For Stages 1 to 3, the wind forces and moments acting on the car-body are:

$$\begin{cases} F_y = \beta\left(F_{y0} + F_{y1}\right) \\ F_z = \beta\left(F_{z0} + F_{z1}\right) \\ M_x = \beta\left(M_{x0} + M_{x1}\right) + \left(z - \dfrac{H_c}{2}\right)F_y \\ M_y = -\left(x - \dfrac{S_c}{2}\right)F_z \\ M_z = \left(x - \dfrac{S_c}{2}\right)F_y \end{cases} \tag{6}$$

For Stage 4, the forces and moments acting on the car-body are the sum of respective forces and moments acting on the rear and the front areas exposed to the wind

$$\begin{cases} F_y = F_{yR} + F_{yF} = \beta_R\left(F_{y0} + F_{y1}\right) + \beta_F\left(F_{y0} + F_{y1}\right) \\ F_z = F_{zR} + F_{zF} = \beta_R\left(F_{z0} + F_{z1}\right) + \beta_F\left(F_{z0} + F_{z1}\right) \\ M_x = \left(\beta_R + \beta_F\right)\left(M_{x0} + M_{x1}\right) + \left(z_R - \dfrac{H_c}{2}\right)F_{yR} + \left(z_F - \dfrac{H_c}{2}\right)F_{yF} \\ M_y = -\left(x_R - \dfrac{S_c}{2}\right)F_{zR} + \left(x_F - \dfrac{S_c}{2}\right)F_{zF} \\ M_z = \left(x_R - \dfrac{S_c}{2}\right)F_{yR} - \left(x_F - \dfrac{S_c}{2}\right)F_{yF} \end{cases} \tag{7}$$

3. Model of wind-vehicle-bridge

It is assumed in the wind-vehicle-bridge system that:

(1) Each vehicle of the train is independent and composed of one car body, two bogies, 4 or 6 wheel-sets, and spring-damper suspensions between the above components.

(2) Based on Kalker's linear theory, the wheel-rail lateral interaction force is in proportion to the wheel-rail relative velocity.

(3) Based on the wheel-rail corresponding assumption, the wheels and the rail have the same vertical and rotational displacements at the wheel-rail contact point.

According to the authors' previous work (Xia and Zhang 2005, Zhang and Xia 2013), the equilibrium equations can be expressed as

$$\begin{cases} \mathbf{M}_v\ddot{\mathbf{X}}_v + \left(\mathbf{C}_v + \mathbf{C}_c\right)\dot{\mathbf{X}}_v + \mathbf{K}_v\mathbf{X}_v = \mathbf{F}_{vi} + \mathbf{F}_{vs} + \mathbf{F}_{vb} \\ \mathbf{M}_b\ddot{\mathbf{X}}_b + \mathbf{C}_b\dot{\mathbf{X}}_b + \mathbf{K}_b\mathbf{X}_b = \mathbf{F}_{bi} + \mathbf{F}_{bg} + \mathbf{F}_{bs} + \mathbf{F}_{bb} \end{cases} \tag{8}$$

where $\mathbf{M}_v$, $\mathbf{C}_v$, and $\mathbf{K}_v$ are the mass, dumping, and stiffness matrices of the vehicle subsystem, respectively. $\mathbf{M}_b$, $\mathbf{C}_b$, and $\mathbf{K}_b$ are the mass, dumping and stiffness matrices of the bridge subsystem,

respectively. $\mathbf{C}_c$ is the additional damping matrix induced by the wheel-rail lateral interaction. $\mathbf{F}_{vi}$ and $\mathbf{F}_{bi}$ are the wheel-rail interaction forces induced by the track irregularities. $\mathbf{F}_{bg}$ is the static gravity load of vehicle on the bridge. Details of the above matrices and force vectors can be found in Zhang and Xia (2013). The force vectors $\mathbf{F}_{vs}$ and $\mathbf{F}_{bs}$ are the static wind load of the vehicle and the bridge, respectively, calculated by Eq. (1). The force vectors $\mathbf{F}_{vb}$ and $\mathbf{F}_{bb}$ are the buffeting wind load of the bridge and the vehicle, respectively, calculated by Eq. (2).

With two interacting subsystems, the vehicle-bridge coupled system must be solved with an iterative procedure. It is not unconditional convergent, as concluded by Zhai (2013). In order to improve convergence results, an inter-history iteration procedure was developed to solve Eq. (8). The following steps were conducted:

(1) Solving the vehicle subsystem by assuming the bridge subsystem rigid, setting the bridge motion to zero, acting the wind load on the car-body, and adopting the track irregularities as the excitation, to obtain the time histories of wheel-rail forces and moments for all wheel-sets;

(2) The bridge subsystem equations were solved by applying the wheel-rail interaction force histories obtained in the previous step combined with the wind load on the bridge deck to obtain the updated time histories of bridge deck motion.

(3) The vehicle subsystem equations were solved by combining the updated bridge deck movements obtained in Step 2 with the updated track irregularity excitations to obtain the updated time histories of wheel-rail forces and moments for all wheel-sets under the wind load.

(4) The convergence errors of wheel-rail interaction force histories were calculated. If convergence was obtained, the calculation was complete. Otherwise, the current results were used in Step 2 and another iteration was conducted.

It should be noted that the wind loads are functions of the train location X and time t, but not functions of the bridge or vehicle motion. Therefore, the wind loads can be calculated before iteration steps. On the other hand, the interaction forces $\mathbf{F}_{vi}$ and $\mathbf{F}_{bi}$ are functions of the wheel-rail relative motions and thus must be re-calculated in each iteration step.
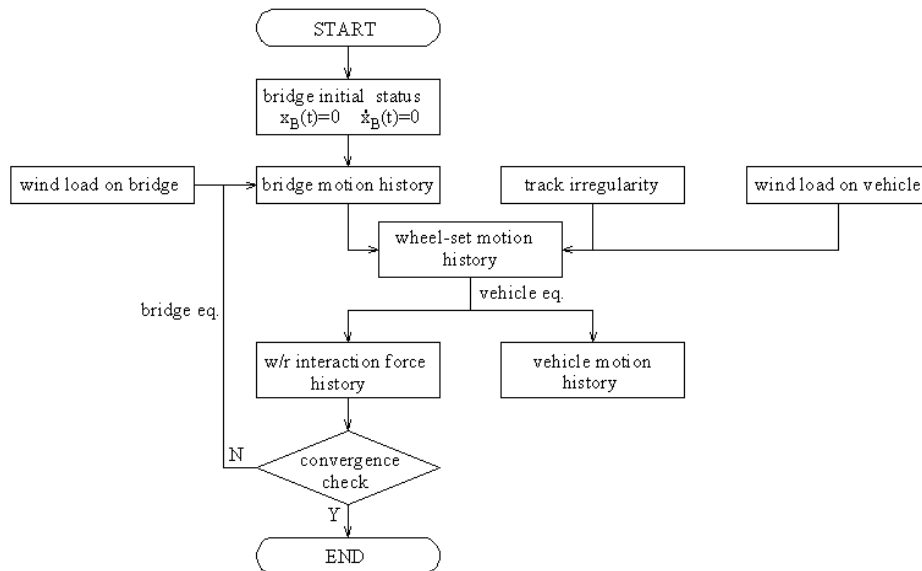

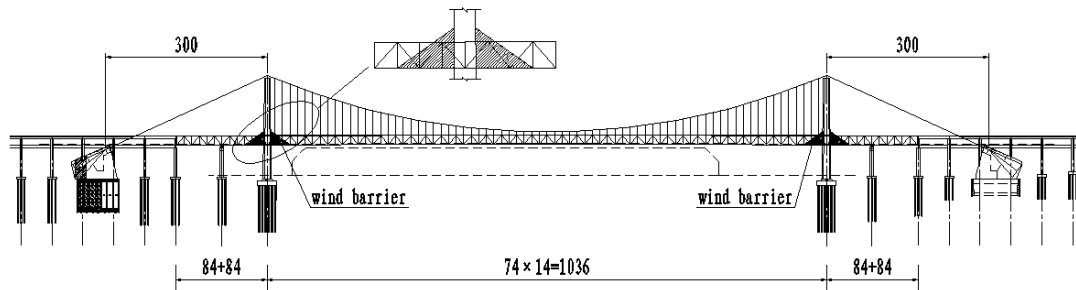Fig. 3 Procedure of inter-history iteration considering wind load
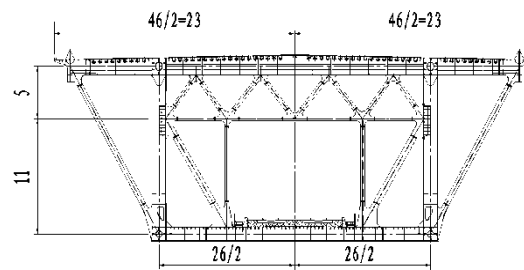
Fig. 4 Main dimensions of the bridge (m)

Fig. 5 Cross section of the bridge (m)

4. Case study

A CRH2 high-speed train running through a suspension bridge is considered with a wind velocity of 20 m/s and train speeds of 120 km/h, 160 km/h, and 200 km/h. The bridge has spans of (84+84+1036+84+84) m, whose dimensions and possible wind barrier design are shown in Fig. 4. The cross section is shown in Fig. 5.

The CRH2 train has 8 vehicles composed of MTMTTMTM, where M is a tractor car and T is a trailer car. The parameters of the train vehicles are listed in Table 4.

Table 4 Parameters of train

Item	Unit	Tractor	Trailer
Length of vehicle, S_c	m	25	25
Height of vehicle, H_c	m	3.7	3.7
Distance between bogies	m	17.5	17.5
Distance between wheel sets	m	2.5	2.5
Axial Load	kN	135	120

The wind velocity field is generated from the Spectra expressed in Eq. (9). The track irregularity samples are generated from the German Low Disturb Spectra, expressed in Eq. (10). These spectra are commonly used in vehicle-bridge interaction analyses for high-speed railways in Chinese and European railway systems (Zhai 2013, Zhang 2013).

$$\begin{cases} S_u(n) = \dfrac{200 f(z) u_*^2}{n[1 + 50 f(z)]^{5/3}} \\[3mm] S_\omega(n) = \dfrac{6 f(z) u_*^2}{n[1 + 4 f(z)]^2} \end{cases} \tag{9}$$

$$\begin{cases} S_a(\Omega) = \dfrac{A_a \cdot \Omega_c^2}{(\Omega^2 + \Omega_r^2)(\Omega^2 + \Omega_c^2)} \\[3mm] S_v(\Omega) = \dfrac{A_v \cdot \Omega_c^2}{(\Omega^2 + \Omega_r^2)(\Omega^2 + \Omega_c^2)} \\[3mm] S_c(\Omega) = \dfrac{A_v \cdot b^{-2} \cdot \Omega_c^2 \cdot \Omega^2}{(\Omega^2 + \Omega_r^2)(\Omega^2 + \Omega_c^2)(\Omega^2 + \Omega_s^2)} \end{cases} \tag{10}$$

The lateral and vertical fluctuating wind velocity histories at the bridge mid span for the average wind velocity of 20 m/s are shown in Fig. 6. The aerodynamic parameters are obtained from CFD calculations (Wang 2010) and are listed in Table 5.
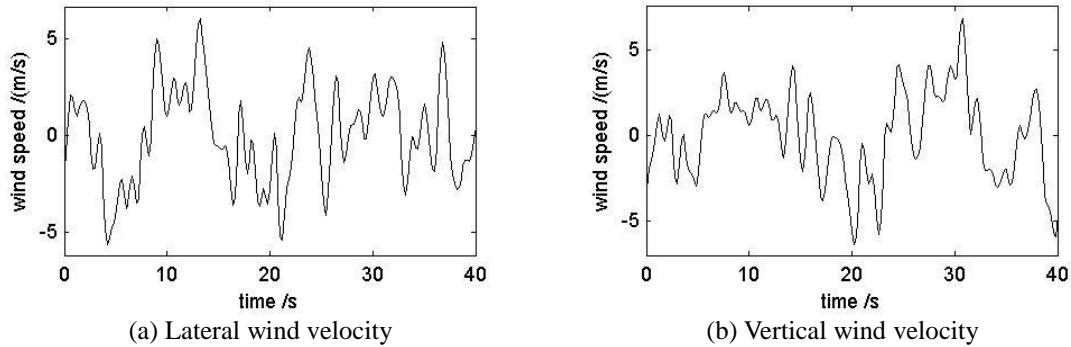

(a) Lateral wind velocity   (b) Vertical wind velocity

Fig. 6 Fluctuating wind velocity histories (U=20 m/s)

Table 5 Aerodynamic parameters

Item	C_D	C_L	C_M	C'_D	C'_L	C'_M
Bridge	0.904	0.301	0.044	0.127	9.827	0.971
Vehicle	0.740	0.821	0.967	--	--	--

The aerodynamic parameters are assumed constant along the deck beam, including the wind barrier area, because the stiffness of the tower is quite large and the deck beam and tower are fixed in the lateral, vertical, and torsional directions. It is calculated by the bridge FEM model that the lateral, vertical, and torsional stiffness at the tower-beam joint are 46, 1001, and 221 times of those at mid-span of the bridge, respectively. The wind barrier areas are near the beam-tower joint, therefore the additional dynamic responses due to the wind barrier under the wind load is very small compared to other parts of the bridge. Errors due to ignoring the wind load on the wind barrier area are therefore considered acceptable.

When wind barriers higher than the vehicle height are used, the shielded area on the vehicle will still be equal to the vehicle side area. When wind barriers that are lower than the vehicle height are used, a constant torsional moment acts on the car-body, which may increase the possibility of derailment or overturning. These two choices of barrier height are undesirable. Therefore, the height of the wind barrier was chosen as the vehicle height, H_c, in the case study. Barrier lengths from 10 m to 50 m are analyzed, and the case without a wind barrier was also analyzed as a baseline. The vibration amplitudes and accelerations of the bridge at the mid span, the derailment factors, offload factors, and car-body accelerations of the train vehicles were calculated for each case.

The maximum and minimum bridge responses with 0-50 m wind barrier lengths under different train speeds are listed in Table 6. It is obvious that the bridge vibration changes little with different sizes of wind barrier size. This is because the wind barriers are relatively small and the wind loads on them are insignificant compared to the loads on the bridge deck induced by the wind and the dynamic loads of the train. An additional reason for the small contribution of the wind barrier to the bridge vibration is that the wind barriers are near the bridge tower, whose stiffness is much larger than the other parts of the suspension bridge. Thus, a large proportion of barrier wind loads are transferred to the bridge tower, not to the deck system.

Fig. 7 shows the running safety factors of the train when it runs through the tower with triangular barriers of different lengths. Compared in Figs. 8 and 9 are, as typical cases, with respect to barrier lengths 0 m, 10 m and 40 m with train speed of 200 km/h, the derailment factor and offload factor histories of the 19th wheel-set, whose arrival time at the centers of the bridge tower sections is 17.586 s and 36.234 s, respectively.

The derailment factor is defined as the ratio of the lateral wheel-rail force and the vertical wheel-rail force at a certain wheel-rail contact point (referring to the left or right wheel of the wheel set). The offload factor is defined as the ratio of the offload and the static wheel load at a certain wheel-rail contact point. For a wheel set

Table 6 Bridge responses with 0-50 m wind barrier

Item	Unit	120 km/h	160 km/h	200 km/h
Vertical amplitude, mid span	mm	106.9~107.0	107.4~107.5	109.3~109.4
Lateral amplitude, mid span	mm	119.8~120.1	120.0~120.2	120.6~120.9
Vertical acceleration, mid span	m/s2	55.3~55.4	56.3~56.5	59.5~59.7
Lateral acceleration, mid span	m/s2	62.4~62.8	63.6~63.9	63.8~64.0

$$\text{Derailment factor: } \frac{Q}{P} = \max\left(\frac{Q_1}{P_1}, \frac{Q_2}{P_2}\right) \tag{11}$$

$$\text{Offload factor: } \frac{\Delta P}{P} = \max\left(\frac{P_{st} - P_1}{P_{st}}, \frac{P_{st} - P_2}{P_{st}}\right) \tag{12}$$

where P_1 and P_2 are the vertical wheel-rail force at left and right wheel-rail contact points, respectively. Q_1 and Q_2 are lateral wheel-rail force at left and right wheel-rail contact points, respectively. P_{st} is the static wheel load, which is half of the axis load.

As shown in Fig. 8, the derailment factor varies little among the cases with different size of wind barrier. This is due to the vibration attenuation effect of the train. The sudden wind load induced by the barriers has limited energy and a very short duration: 0.27 s for 200 km/h and 0.45 s for 120 km/h. Therefore, the induced vibration is damped by the suspension system of the train vehicle. The effects from the shielding effect are less as compared to random factors such as the track irregularities and the fluctuating components of the wind, and can not be found are contained in the derailment factor histories.

As shown in Fig. 9, the offload factor decreased slightly in the bridge tower sections. This is because the lateral wind load has a constant rolling trend (rotation about the x-axis), which causes the offload of the wheel on the windward side.
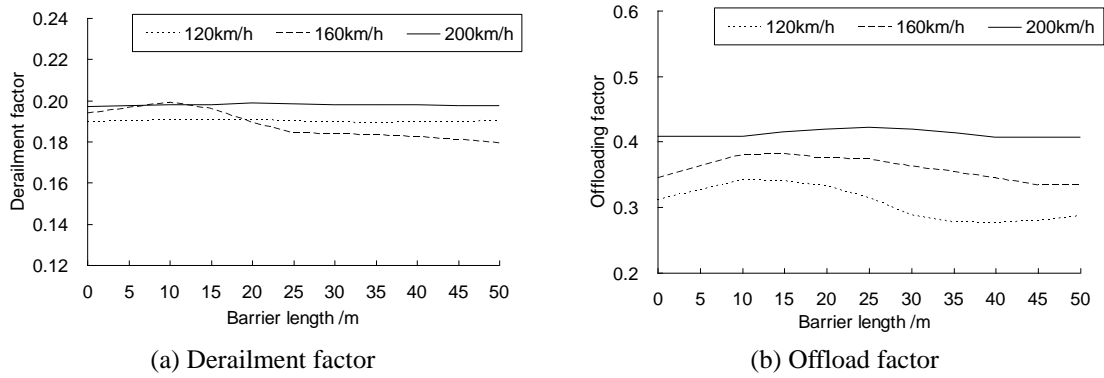

(a) Derailment factor   (b) Offload factor

Fig. 7 Vehicle safety factors with respect to different barrier lengths

(a) S_b=0 m   (b) S_b=10 m   (c) S_b=40 m

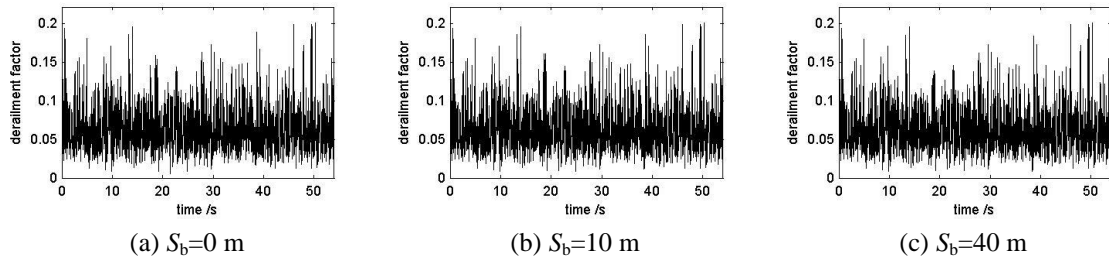Fig. 8 Derailment factor histories

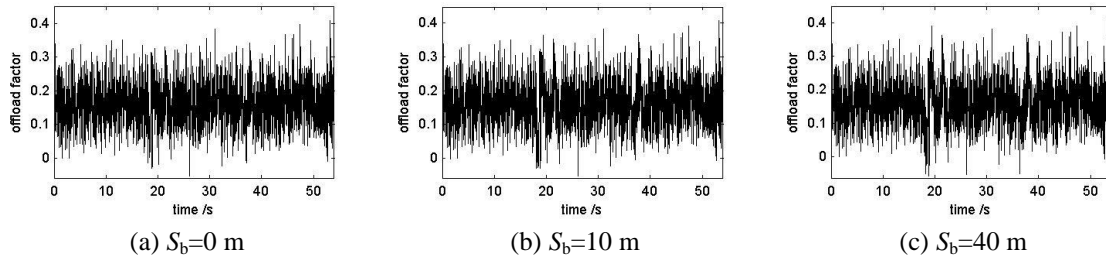(a) S_b=0 m   (b) S_b=10 m   (c) S_b=40 m

Fig. 9 Offload factor histories

This is due to the shielding effect of the bridge tower and wind barrier, which reduces the area subjected to the wind. Thus, the offload factor is temporarily decreased and the maximum value of the offload factor over the entire time history does not change.

The maximum derailment and offload factors in each stage for the 19th wheel-set are plotted in Figs. 10 and 11. SnTm represents the nth Stage when the train transverses the bridge Tower number m. Stages 1, 2, 6 and 7 are neglected for the case S_b=10 m and Stages 2 and 6 are neglected for the case S_b=10 m, based on the equations in Table 2. From the figures, it is seen that the derailment and offload factors decrease slightly from a larger wind barrier within Stages 3, 4, and 5. An important caveat is that the safety factors are affected by the random action of wind; therefore, the current trends may differ with a different wind speed history field.
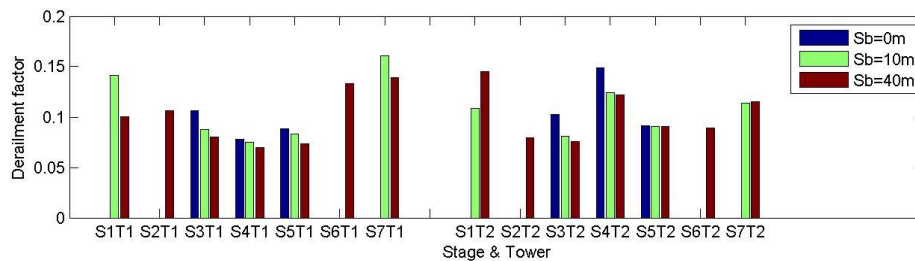

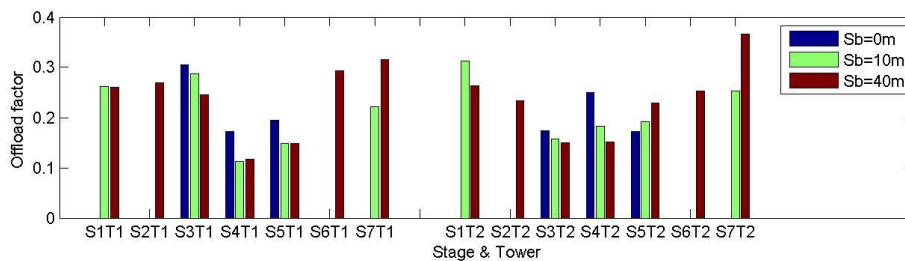Fig. 10 Maximum derailment factor in each stage
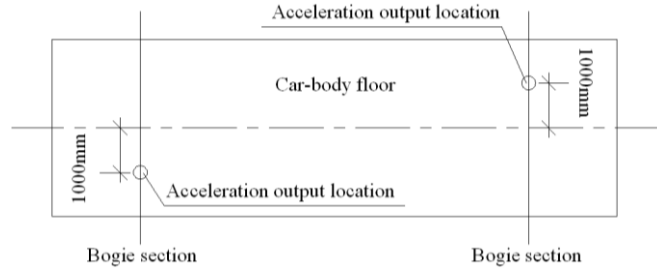

Fig. 11 Maximum offload factor in each stage

Fig. 12 Output locations of car-body accelerations

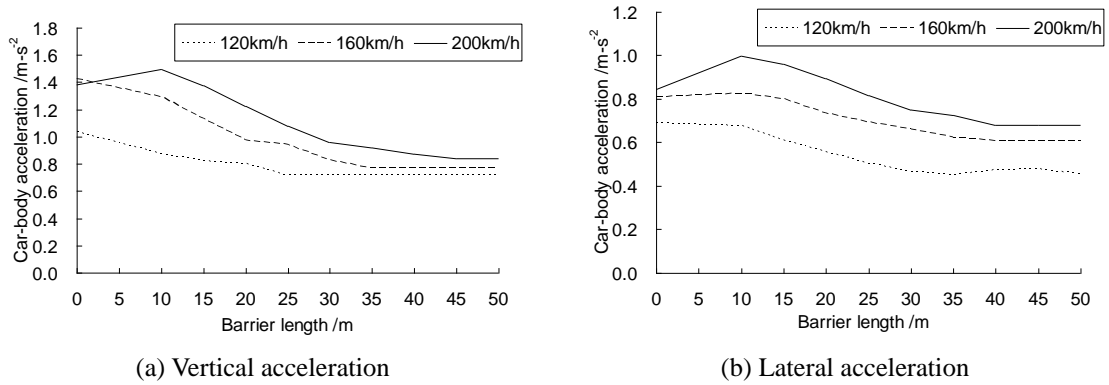(a) Vertical acceleration   (b) Lateral acceleration

Fig. 13 Car-body acceleration vs. barrier length

Based on Item 4.2.1 of the Chinese Code *Railway Vehicles Specification for Evaluation the Dynamic Performance and Accreditation Test* (GB5599-85), the car-body acceleration output location is on the floor of the section, which is laterally offset 1,000 mm from the longitudinal axis as shown in Fig. 12. The maximum accelerations at this location as a function of barrier length are shown in Fig. 13.
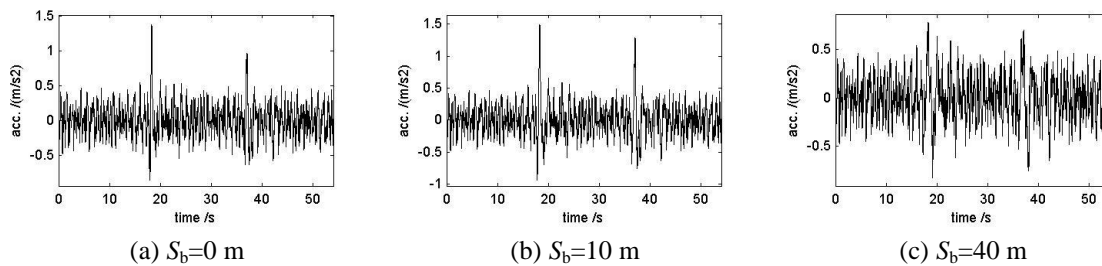

(a) S_b=0 m   (b) S_b=10 m   (c) S_b=40 m

Fig. 14 Vertical acceleration histories at output location

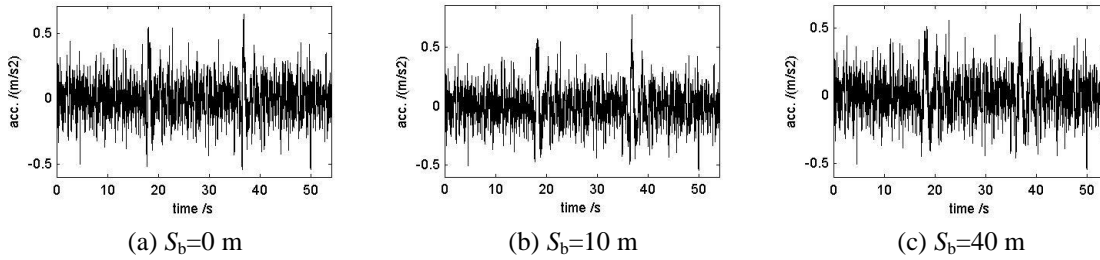(a) S_b=0 m   (b) S_b=10 m   (c) S_b=40 m

Fig. 15 Lateral acceleration histories at output location

The results show a general trend of decreasing car-body vibration as the size of the wind barrier increases. The exception is with the first 10 m of wind barrier heights. To explain this exception, the acceleration histories of the 5th car-body at a train speed of 200 km/h are compared for different barrier lengths in Figs. 14 and 15. The peak acceleration values appear at 17.901 s and 36.549 s, which correspond to the arrival times of the wheel sets at the centers of the first and second bridge tower sections, respectively.

The vertical acceleration at the output location is the sum of the vehicle's vertical, rolling (rotation about x-axis), and nodding (rotation about y-axis) components. The lateral acceleration is the sum of the vehicle's lateral, rolling, and yawing (rotation about z-axis) components. In order to further analyze the peak values with different barrier lengths, the histories of the vehicle lateral, rolling, nodding, and yawing accelerations at the vehicle center are shown in Fig. 16 to Fig. 21.
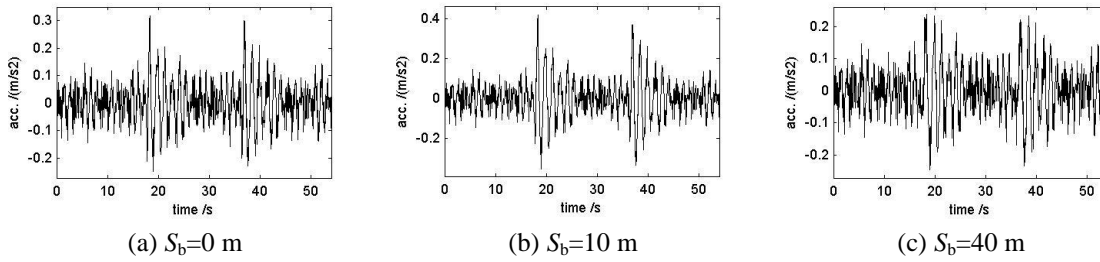

(a) S_b=0 m   (b) S_b=10 m   (c) S_b=40 m

Fig. 16 Vertical acceleration histories at vehicle center

(a) S_b=0 m   (b) S_b=10 m   (c) S_b=40 m
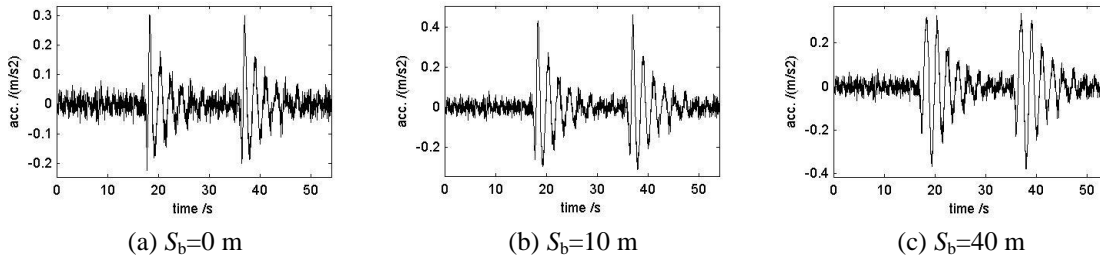
Fig. 17 Rolling component in vertical acceleration at output location

(a) S_b=0 m   (b) S_b=10 m   (c) S_b=40 m
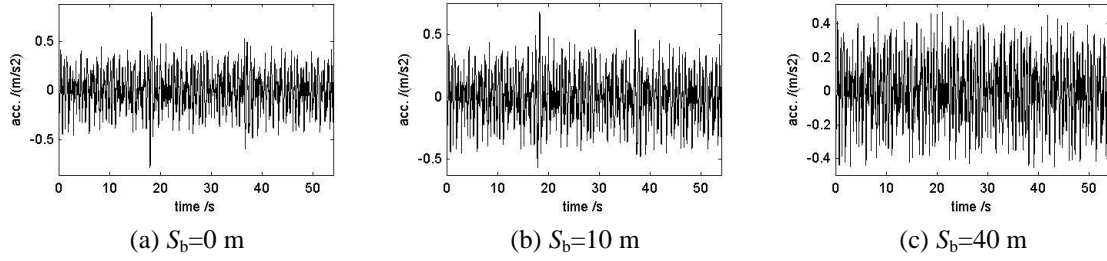
Fig. 18 Nodding component in vertical acceleration at output location

(a) S_b=0 m   (b) S_b=10 m   (c) S_b=40 m
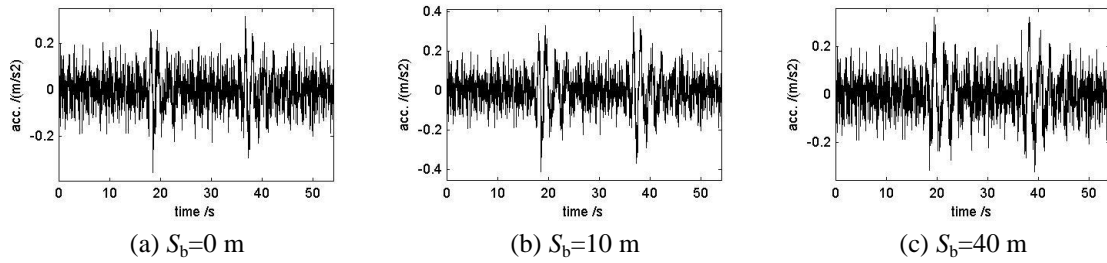
Fig. 19 Lateral acceleration histories at vehicle center

(a) S_b=0 m   (b) S_b=10 m   (c) S_b=40 m
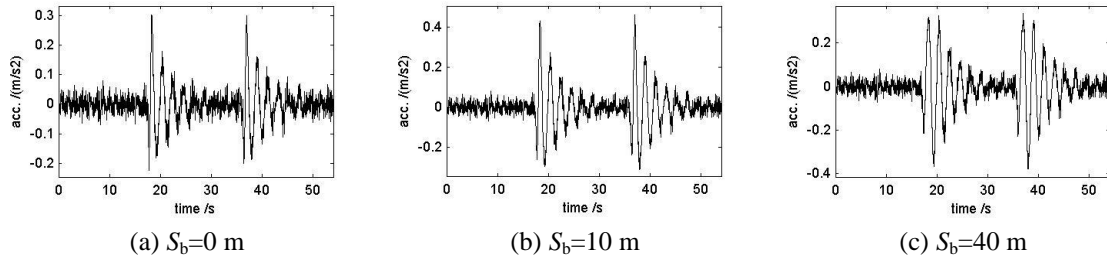
Fig. 20 Rolling component in lateral acceleration at output location

(a) S_b=0 m   (b) S_b=10 m   (c) S_b=40 m
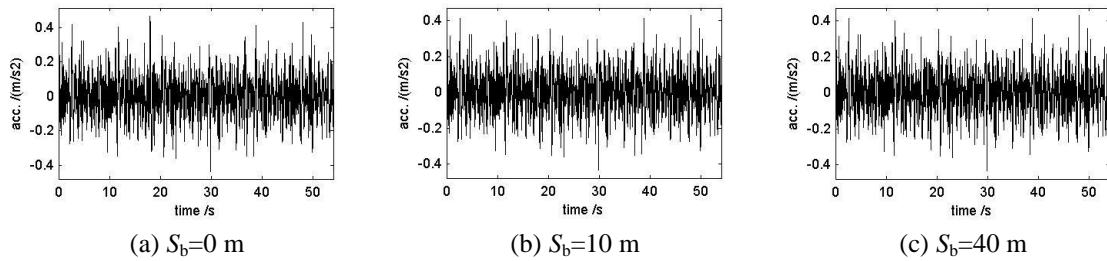
Fig. 21 Yawing component in lateral acceleration at output location

It is seen in Figs. 18 and 21 that the peaks in the nodding and yawing components are not dominant. This is due to the relative large inertia about the y- and z-axes. For the case of the 10 m wind barrier, the vertical, lateral, and rolling motions are larger than those in the case without wind barrier. Therefore, the acceleration responses at the output location are larger. In the case of the 40 m wind barrier, peaks in the vertical and lateral components at the tower locations are notably absent; the rolling component is approximately equal to that in the case without wind barrier. Thus, the acceleration responses at the output location are much lower.

From Figs. 16 and 19 it is apparent that the vertical and lateral motions with a 10 m wind barrier are larger than without a wind barrier. On one hand, the triangular transition part of the wind barrier reduces the impact of the shielding effect. On the other hand, the shielded area of vehicle is increased by the wind barriers relative to the case without a wind barrier, and the larger shielding area enlarges the variation of the wind load on the train running through. Especially when the barrier length is small, the enlarge effect is more important than the reduction effect.

In the case of a 10 m wind barrier, the wind barrier is not long enough; the contribution of the eccentricity of the lateral action is greater than the torsional action, so the rolling motion is larger than the case without wind barrier, as compared in Figs. 17 and 20. This can be explained with reference to Eq. (3), in which the rolling moment in the third equation comes from the vehicle torsional action (the first 2 terms) and the eccentricity of the lateral action (the final 2 terms). The shielding effect decreases the vehicle torsional action. However, since only the lower part of the vehicle is shielded, the center of the wind-subjected area is raised, which enlarges the arm z_A and then the rolling moment M_x of the lateral wind action.

The maximum vertical and lateral accelerations in each stage for the 5th vehicle are plotted in Figs. 22 and 23. It is apparent that the 40 m wind barrier has the lowest car-body accelerations in both vertical and lateral directions for most stages.
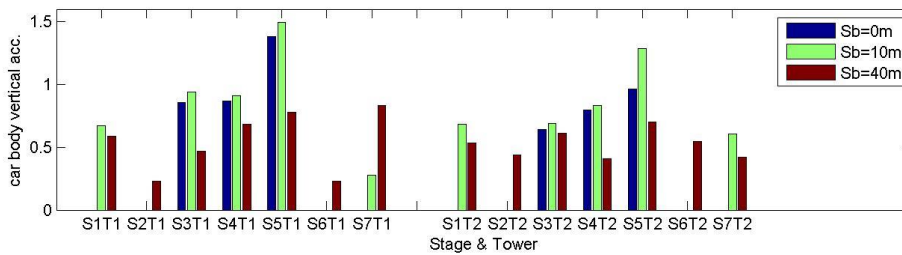

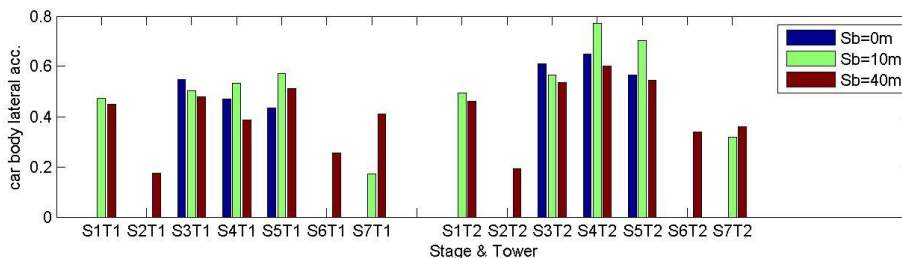Fig. 22 Maximum vertical acceleration in each stage

Fig. 23 Maximum lateral acceleration in each stage

These results indicate that the sudden impact of a wind load induced by the bridge tower and wind barrier has a slight effect on the vibrations of the bridge and the running train. There is also a noticeable effect on the car-body accelerations. A triangular wind barrier with enough size creates an effective transition to significantly decrease the car-body peak accelerations. For the case study used here, a triangular wind barrier with 40 m length and 3.7 m height is found to be the best configuration. This resulted the car-body peak acceleration reduction of 31-37% in the vertical direction and a 19-31% reduction in the lateral direction, depending on the train speed.

5. Conclusions

A method to analyze the wind-vehicle-bridge coupled system has been proposed which considers the shielding effect of the bridge tower and triangular wind barriers. The wind shielding effect is assumed to act uniformly over the car-body body. The inter-history iteration method is adopted to solve the vehicle-bridge dynamic equilibrium equations with an external wind load. The case of a high-speed train traveling through a long-span suspension bridge under a wind load is analyzed with the following conclusions:

- The sudden impact of a wind load induced by the bridge tower and wind barrier has an obvious effect on the car-body accelerations, yet a slight effect on the bridge and train vibrations.
- A wind barrier with sufficient size is able to provide an effective transition to mitigate the induced wind from a bridge tower obstacle, resulting in a significant decrease in the car-body peak accelerations.
- A triangular wind barrier with 40 m length and 3.7 m height is recommended for a bridge tower of 15 m width. The analysis showed that this barrier reduced the car-body peak accelerations by 31-37% in the vertical direction and 19-31% in lateral direction for train speeds of 120-200 km/h.

References

Baker, C.J. (1991a), "Ground vehicles in high cross winds Part I: Steady aerodynamic forces", *J. Fluid. Struct.*, **5**(1), 69-90.
Baker, C.J. (1991b), "Ground vehicles in high cross winds Part II: Unsteady aerodynamic forces", *J. Fluid. Struct.*, **5**(1), 91-111.
Baker, C.J. (1991c), "Ground vehicles in high cross winds Part III: The interaction of aerodynamic forces and the vehicle system", *J. Fluid. Struct.*, **5**(2), 221-241.
Cai, C.S., Liu, X.Z., Peng, W., *et al.* (2013), "Framework of wind-vehicle-bridge interaction analysis and its applications", *J. Earthq. Tsunami*, **7**(3), 1350020.

Cao, Y.H., Xiang, H.F. and Zhou, Y. (2000), "Simulation of stochastic wind velocity field on long-span bridges", *Eng. Mech.*, **126** (1), 1-6.

Chen, Z.W., Xu, Y.L., Li, Q. and Wu, D.J. (2011), "Dynamic stress analysis of long suspension bridges under wind railway and highway loadings", *J. Bridge Eng.*, **16**(3), 383-391.

Domaneschi, M. and Martinelli, L. (2014), "Refined optimal passive control of buffeting-induced wind loading of a suspension bridge", *Wind Struct.*, **18**(1), 1-20.

Gao, Z.Y. (2014), "Pingtan Strait Highway-railway Bridge under complex marine condition", *Keynote report collections of International Bridge Science & Technology Forum*, Wuhan, 143-172.

Ge, Y.J. and Zhao L. (2014), "Wind-excited stochastic vibration of long-span bridge considering wind field parameters during typhoon landfall", *Wind Struct.*, **19**(4), 421-441.

Guo, W.W., Xia, H. and Xu, Y.L. (2010), "Running safety analysis of a train on the Tsing Ma Bridge", *Earthq. Eng. Eng. Vib.*, **9**(3), 307-318.

Han, Y., Hu, J.X, Cai, C.S. and Chen, Z. and Li, C. (2012), "Experimental and numerical studies of aerodynamic forces on vehicles and bridges", *Wind Struct.*, **17**(2), 163-184.

Kim, B.C. and Yhim, S.S. (2014), "Buffeting analysis of a cable-stayed bridge using three-dimensional computational fluid dynamics", *J. Bridge Eng.*, **19**(11), 04014044.

Li, Y.L., Hu, P., Xu, Y.L., Zhang, M.J. and Liao, H. (2014),"Wind loads on a moving vehicle–bridge deck system by wind-tunnel model test", *Wind Struct.*, **19**(2), 145-167.

Li, Y.L., Qiang, S.Z., Liao, H.L. and Xu, Y.L. (2005), "Dynamics of wind-rail vehicle-bridge systems", *J. Wind Eng. Ind.Aerod.*, **93**, 483-507.

Li, Y.L., Xiang, H.Y., Wang, B., Xu, Y.L. and Qiang S.Z. (2013), "Dynamic analysis of wind-vehicle-bridge coupling system during the meeting of two trains", *Adv. Struct. Eng.*, **16**(10), 1663-1670.

Lin, Y.K. and Yang, J.N. (1983), "Multimode bridge response to wind excitations", *Engineering Mechanics*, ASCE, **109**(2), 586–603.

Wang, B., Xu, Y.L., Zhu, L.D. and Li Y.L. (2014a), "Crosswind effects on high-sided road vehicles with and without movement", *Wind Struct.*, 18(2), 155-180.

Wang, B., Xu, Y.L., Zhu, L.D. and Li Y.L. (2014b), "Crosswind effect studies in road vehicle passing by bridge tower using computational fluid dynamics", *Eng. Appl. Comput. Fluid Mech.*, **8**(3), 330-344.

Wang, S. (2012), *Dynamic analysis of long-span bridge subjected to cross wind and train*, Beijing Jiaotong University, Beijing.

Xia, H. and Zhang, N. (2005), "Dynamic analysis of railway bridge under high speed trains", *Comput. Struct.*, **83**(23-24), 1891-1901.

Xu, Y.L. and Zhu, L.D. (2005), "Buffeting response of long-span cable-supported bridges under skew winds. Part 2: Case study", *J. Sound Vib.*, **281**(3-5), 675-697.

Xu, Y.L., Zhang, N. and Xia, H. (2004), "Vibration of coupled train and cable stayed bridge system in cross wind", *Eng. Struct.*, **26**(10), 1389-1406.

Zhai, W.M., Xia H., Cai, C.B., *et al.* (2013), "High-speed train-track-bridge dynamic interactions - Part I: theoretical model and numerical simulation", *Int. J. Rail Transportation*, **1**(1-2), 3-24.

Zhang, N. and Xia, H. (2013), "Dynamic analysis of coupled vehicle–bridge system based on inter-system iteration method", *Comput. Struct.*, **114-115**, 26-34.

Zhang, W.M., Ge, Y.J. and Levitan, M.L. (2011), "Aerodynamic flutter analysis of a new suspension bridge with double main spans", *Wind Struct.*, **14**(3), 187-208.

AD